

Broadband giant nonlinear response from electrically tunable polaritonic metasurfaces

Jaeyeon Yu

Ulsan National Institute of Science and Technology

Seongjin Park

Ulsan National Institute of Science and Technology

Inyong Hwang

Ulsan National Institute of Science and Technology

Daeik Kim

Ulsan National Institute of Science and Technology

Frederic Demmerle

Walter Schottky Institute

Gerhard Boehm

Walter Shottky Institut

Markus-Christian Amann

Technische Universitat Munchen

Mikhail Belkin

Technical University Munich

Jongwon Lee (✉ jongwonlee@unist.ac.kr)

Ulsan National Institute of Science and Technology <https://orcid.org/0000-0002-3878-0650>

Article

Keywords: nonlinear polaritonic metasurfaces, nanoresonators, plasmonic nanocavity

Posted Date: August 14th, 2020

DOI: <https://doi.org/10.21203/rs.3.rs-57822/v1>

License:   This work is licensed under a Creative Commons Attribution 4.0 International License.

[Read Full License](#)

Version of Record: A version of this preprint was published at Nature Photonics on December 23rd, 2021.
See the published version at <https://doi.org/10.1038/s41566-021-00923-7>.

Broadband giant nonlinear response from electrically tunable polaritonic metasurfaces

Jeayeon Yu¹, Seongjin Park¹, Inyong Hwang¹, Daeik Kim¹, Frederic Demmerle², Gerhard Boehm², Markus-Christian Amann², Mikhail A. Belkin², and Jongwon Lee^{1*}

¹School of Electrical and Computer Engineering, Ulsan National Institute of Science and Technology (UNIST), Ulsan 44919, Republic of Korea

²Walter Schottky Institut, Technische Universität München, Am Coulombwall 4, Garching 85748, Germany

**Corresponding author. E-mail: jongwonlee@unist.ac.kr*

Abstract

Optically-thin nonlinear polaritonic metasurfaces created by coupling of intersubband nonlinearities in semiconductor heterostructures with optical modes in nanoresonators have recently demonstrated efficient three-wave-mixing at very low pumping intensities of the order of few tens of kW cm^{-2} . In these subwavelength structures, the efficiency and the spectral bandwidth of the wave mixing depends solely on nonlinearity of the constituent meta-atoms. Here we exploit this property to demonstrate an electrically-tunable nonlinear metasurface that combines a plasmonic nanocavity and a quantum-engineered semiconductor heterostructure, in which the magnitude and the spectral characteristics of the nonlinear response are controlled by bias voltage through the quantum-confined Stark effect. We demonstrate tuning the peak second-harmonic-generation (SHG) efficiency in the range of $8.7 - 10.75 \mu\text{m}$ and modulation of SHG intensity at a fixed pump wavelength by applying bias voltage. An SHG power conversion efficiency of 0.082% was achieved using a peak pump intensity of only 80kW cm^{-2} .

Metasurfaces constructed through a two-dimensional array of engineered subwavelength structures, capable of controlling local scattering amplitude, phase, and polarization states, have opened an entirely new way of manipulating light¹. In the past decade, researches on electrically reconfigurable metasurfaces that can overcome the static limit of passive flat optics have been of particular interest, since they can provide a platform enabling dynamic manipulation of light and on-chip integration with other electronics². Based on electrically reconfigurable linear metasurfaces, interesting applications, such as intensity and phase modulation³⁻⁵, dynamic beam-shaping⁶⁻⁸, varifocal lenses⁸, and programmable holography⁹, have been demonstrated.

As a linear counterpart, nonlinear metasurfaces that generate nonlinear optical responses in engineered subwavelength-thin films open new avenues for flat nonlinear optics that can have significant advantages over bulk nonlinear crystals such as relaxed phase-matching constraint and the ability to engineer local nonlinear responses at a deep subwavelength scale¹⁰⁻¹³. Nonlinear metasurfaces provide new possibilities for innovative applications, including nonlinear holography¹⁴⁻¹⁸, optical encryptions¹⁹⁻²¹, nonlinear optical switching and modulation^{22, 23}, and applications for generating new frequencies based on nonlinear frequency mixing¹³. To realize such applications, various nonlinear platforms using plasmonic²⁴⁻²⁶ or dielectric structures^{18, 27-30} for efficient second or third harmonic generation (SHG or THG) in subwavelength films have been proposed. However, these structures are mostly composed of passive resonators using materials with intrinsically low nonlinear response, thus requiring a high-power ultrafast laser and limiting the electrical tuning of nonlinear response. Only a few studies employing plasmonic or dielectric metasurfaces demonstrated electrical modulation of nonlinear response based on electric-field-induced SHG or optical rectification³¹⁻³⁴.

Recently, a nonlinear intersubband polaritonic metasurfaces comprised of plasmonic nanocavities filled with a multiple quantum well (MQW) layer with giant nonlinear optical responses were studied³⁵⁻⁴⁰. Owing to the resonant nonlinearities associated with intersubband transitions (ISTs) between electron subbands in an n-doped conduction band of a semiconductor heterostructure, the MQW structures can produce giant 2nd and 3rd order nonlinear responses for the optical field polarized along vertical (z) direction with respect to semiconductor layers ($\chi_{zzz}^{(2)}$ and $\chi_{zzzz}^{(3)}$, respectively)⁴¹. The values of these nonlinearities can be up to 4 - 5 orders of magnitude higher than that in natural nonlinear materials. Giant intersubband nonlinear response of MQW systems enables efficient frequency conversion in the nonlinear intersubband polaritonic metasurfaces using only moderate pump intensities of approximately few tens of kW cm⁻² and SHG conversion efficiency of as high as 0.08 % was reported using a peak pump intensity of only 11 kW cm⁻² in the mid-infrared (MIR) range³⁸. An ability to electrically tune the nonlinear response of the meta-atoms in the intersubband polaritonic metasurfaces allows one to extend their optical bandwidth and to control and modulate nonlinear response at the individual nanoresonators level.

Here, we employ Stark tuning of intersubband nonlinearities⁴² to demonstrate for the first time the electrically tunable nonlinear response in the intersubband polaritonic metasurfaces. The MQW structure used in this work comprises a coupled three-quantum-well system in which three electron subbands are predominantly confined and controlled in each quantum well with different well widths, and broadband giant $\chi_{zzz}^{(2)}$ can be induced through the quantum confined Stark effect (QCSE). By combining plasmonic nanocavity structures capable of generating SHG in free-space and applying bias voltages to the MQW layer, broadly tunable efficient SHG was achieved in the MIR region for the input pump wavelength range of 8-11 μm .

Results

Active nonlinear metasurface based on Stark tuning of intersubband nonlinearities. The concept underlying the operation of our electrically tunable nonlinear metasurface is illustrated in Fig. 1. The metasurface was constructed using an array of plasmonic nanocavity meta-atoms, with a 400-nm-thick MQW layer sandwiched between a top Au plasmonic nanoantenna and a bottom Au ground plane. The two metallic layers within the plasmonic nanocavity were used as contact layers for applying bias voltages to the MQW layer. In this configuration, SHG is produced in reflection and the maximum second harmonic (SH) wavelength is tuned by the bias voltage applied to the metasurface. In addition, it is possible to strongly modulate the SH signal generated from the metasurface at a fixed pump wavelength by using an applied voltage pulse. Electrical tuning of the SHG is achieved through Stark tuning of the intersubband nonlinearity of the MQW structure. Fig. 2a shows the unbiased (0V) conduction band diagram for a single period of the MQW structure, with four quantized electron subbands designed for the electrical tuning of the giant 2nd order nonlinear response. The MQW layer was designed by repeating the coupled three-quantum-well structure twenty times using In_{0.53}Ga_{0.47}As/Al_{0.48}In_{0.52}As heterostructures, where first and fourth, second, and third electron subband are confined predominantly to the left, middle, and right well, respectively. In this structure, the IST energy, E_{ij} , between electron subbands i and j can be tuned according to the bias voltage applied to the MQW layer through the QCSE. Supplementary Figs. 1a and 1b present the conduction band diagrams corresponding to applied bias voltages of +4V and -4V, respectively, over the 400 nm-thick MQW layer. The associated IST energies are shown in Supplementary Fig. 1c. The giant 2nd order nonlinear response of the MQW structure is produced principally by the resonant transitions occurring within the first three electron subbands; therefore, the intersubband nonlinear susceptibility tensor element of the MQW as a function of the bias voltage is expressed using the equation⁴³:

$$\chi_{zzz,1-3}^{(2)}(\omega \rightarrow 2\omega, V) \approx \frac{e^3 (N_{e,1} - N_{e,2})}{\epsilon_0} \frac{z_{12}(V)z_{23}(V)z_{31}(V)}{(\hbar\omega_{31}(V) - 2\hbar\omega - i\hbar\gamma_{31})(\hbar\omega_{21}(V) - \hbar\omega - i\hbar\gamma_{21})} \quad (1)$$

where ω is the pump frequency, e is the electron charge, $N_{e,1}$ and $N_{e,2}$ are the averaged electron densities located at the first and second electron subbands, respectively. $\hbar\omega_{ij}(V) = E_{ij}$, $ez_{ij}(V)$, and $\hbar\gamma_{ij}$ denote the IST energy, the transition dipole moment as a function of the bias voltage V , and the linewidth, respectively, for the transition between electron subbands i and j (cf. Supplementary Table 1). Fig. 2b shows the calculated $\chi_{zzz,1-3}^{(2)}$ values as a function of both the bias voltage (ranging from -4V to +4V) and the pump wavelength. At 0 V, the $\chi_{zzz,1-3}^{(2)}$ peak value of 210 nm V⁻¹ occurs at a wavelength of 9.7 μ m. As the positive bias is applied to the MQW layer, the peak wavelength position of $\chi_{zzz,1-3}^{(2)}$ shifts to a shorter wavelength owing to the increased E_{21} and E_{31} (see Supplementary Fig. 1c), with the opposite trend observed for the negative bias. The calculation results indicate that a broadband giant 2nd order nonlinear response exceeding 120 nm V⁻¹ can be induced in the 8 - 11 μ m wavelength range by applying bias voltages. Although the 2nd order nonlinear response modulation of MQW structures by the QCSE has been reported previously⁴², this study represents the first instance of broadband $\chi_{zzz}^{(2)}$ peak tuning based on three quantum wells through the QCSE and its application to electrically tunable nonlinear metasurfaces. The MQW structure includes a fourth electron subband, and the ISTs among the second to fourth level electrons, with a non-zero electron population at the second level ($N_{e,2}$) due to the high doping level and thermal population, can also produce a strong 2nd order nonlinear response, $\chi_{zzz,2-4}^{(2)}$, as shown in Fig. 2c. The $\chi_{zzz,2-4}^{(2)}$ exhibits a relatively weak nonlinear response for the positive bias voltage, but it increases to 22 nm V⁻¹ for wavelengths reaching to 9 μ m as the negative bias voltage increases as a result of the increased IST energies, E_{23} and E_{42} , and their corresponding dipole

elements (see Methods for calculation details). The designed MQW structure was grown by molecular-beam-epitaxy on a semi-insulating InP substrate; its intersubband absorption measurement result is illustrated in Supplementary Fig. 2 with accompanying discussion. The measured E_{12} value was about 10 meV smaller than the calculated value shown in Fig. 2a, forming the intersubband absorption at a longer wavelength of 10.6 μm .

To achieve efficient SHG based on the broadly tunable giant nonlinear response of the MQW, a meta-atom structure was designed, as shown in Fig. 3a. We designed the complementary V-shaped nanoantenna with a gap in the x -direction between the neighboring unit cells in which plasmonic resonances at the fundamental frequency (FF) and SH frequency are tuned easily by adjusting the antenna length (L) and the bending angle (θ). The MQW region without the top Au nanoantenna was etched, which induces the enhanced E_z field mode following the top nanoantenna shape for an input pump beam⁴⁴ and, simultaneously, uniform vertical current injection from the external bias voltage. The meta-atom structure was designed to induce the enhanced local E_z field in the MQW layer at the FF ω (Fig. 3b) and the SH frequency 2ω (Fig. 3c) for x - and y -polarized input beams, respectively. The electrically tunable effective nonlinear susceptibility out of the metasurface can be expressed as³⁵:

$$\chi_{yxx}^{(2)eff}(V) = \chi_{zzz}^{(2)}(V) \left[\int_{V_{MQW}} \xi_{z(y)}^{2\omega}(x, y, z) \xi_{z(x)}^{\omega}(x, y, z) \xi_{z(x)}^{\omega}(x, y, z) dV \right] / V_{unit} \quad (2)$$

where $\xi_{z(i)}^{\omega \text{ or } 2\omega}$ is the E_z field enhancement in the MQW region normalized to the incident E field polarized in the i -direction at the FF ω or the SH frequency 2ω ; V_{unit} and V_{MQW} represent the MQW volumes in the unit cell before and after etching, respectively. In this configuration, the highest effective nonlinear susceptibility out of the metasurface is produced for yxx polarization combination where the first letter refers to the SH polarization and the last two letters refer to the

FF input pump polarization. As shown in Figs. 3b and 3c, a good modal overlap forms at both lateral ends of the meta-atom structure.

To demonstrate the performance of our metasurface experimentally, we fabricated three $100\ \mu\text{m} \times 100\ \mu\text{m}$ two-dimensional arrays (M1, M2, M3) each incorporating slightly different dimensions of the meta-atom structure. According to their dimensions, the metasurfaces M1, M2 and M3 were optimized to wavelengths of 10.6, 9.8, and 9.6 μm , respectively. The device fabrication process is provided in the Methods and illustrated in Supplementary Fig. 3. Scanning electron microscopy images, with top-down and tilted views, and an optical microscopy image of the fabricated M2 metasurface are shown in Fig. 3d-f, respectively. Fig. 3g shows simulated (dashed line) and measured (solid line) linear reflection spectra of the M2 metasurface for x - (black) and y -polarized (red) IR light at normal incidence. For the x -polarized IR light, polaritonic absorption peak splitting⁴⁵ was observed near a wavelength of 10.5 μm , which is caused by a strong coupling of the plasmonic cavity mode and IST and represents a necessary condition for efficient SHG. For the y -polarized illumination, strong absorption was observed near a wavelength of 5 μm , representing another necessary condition for out-coupling of nonlinear polarization generated in the MQW region to free-space due to Lorentz reciprocity⁴⁴. The results of the linear characterization of the M1 and M3 metasurfaces are shown in Supplementary Figs. 4 and 5.

Electrical tuning of linear and nonlinear response of the metasurface. In the metasurface, the absorption peaks from the polaritonic splitting are modulated by the interplay between the electrically tunable ISTs and the fixed resonance of the plasmonic nanoantenna. To confirm the IST tuning and the corresponding polaritonic peak tuning, linear reflection spectra for the three metasurfaces were measured by applying DC bias voltages from -4 V to +4 V with 1 V step as shown in Figs. 4a – 4c. In Figs. 4a and 4b, the polaritonic peak splitting (green and red dashed

curves) due to the strong coupling of the plasmonic resonance and the E_{12} IST was tuned by changing the bias voltage from +4 V to -4 V according to the red-shifted E_{12} IST wavelength (see Supplementary Fig. 1). As the negative bias voltage was increased, additional peak splitting (blue and green dashed curves) resulting from the coupling with the E_{23} IST was also observed. In the case of the M3 metasurface, the coupling with the E_{12} IST was weak because the plasmonic resonance was apart from the E_{12} IST, but the polaritonic splitting due to coupling with the E_{23} IST near a wavelength of $9\mu\text{m}$ was observed as the negative bias increased. These results confirmed that the ISTs tuned by the bias voltage agreed well with the calculation results. Due to the polaritonic coupling effect, which can be controlled via the bias voltage, it is possible to generate broadband efficient SHG in the 8-11 μm pump wavelength range for the three metasurfaces. The linear spectral tuning of the metasurfaces was well matched with -2V shifted simulation results owing to the discrepancy in IST energies between calculation and experiment (see Supplementary Fig. 6). For different bias voltages, linear reflection spectra near the SH frequency for the y -polarized incident light were simulated and measured, as shown in Supplementary Figs. 7 and 8, respectively. The resonant absorption peak near the SH frequency exhibits no spectral tuning regardless of the applied bias voltage. The current-voltage characteristic of the device shown in Supplementary Fig. 9 reveals the formation of Schottky contacts on both sides of the MQW layer, i.e., at the interfaces with the top and bottom metal layers.

For nonlinear optical characterization, a wavelength tunable quantum cascade laser and a calibrated InSb photodetector were used. The optical setup used for the SHG signal measurement is shown in Fig. 5a. By applying bias voltages from -4 V to +4 V with 2 V step, SHG output spectra for the three metasurfaces were measured, with the results shown in Fig. 5b. Each SHG spectrum was normalized to its maximum SHG output signal. Experimentally, broadband SHG spectral peak

tuning for the 10.75 - 8.7 μm input pump wavelength range (930 to 1150 cm^{-1} in wavenumber) was achieved. As the bias voltage was changed from -4 V to +4 V, the SHG spectral peak for the M1 and M2 metasurfaces was blue-shifted, which is consistent with the tendency of the $\chi_{zzz}^{(2)}(V)$ according to the bias voltage (cf. Fig. 2b). For the M3 metasurface by changing the bias voltage from +4V to -4V, relatively broad SHG output spectrum was observed owing to the simultaneous effects of the 1-3 and 2-4 level ISTs, with the peak narrowing gradually and blue-shifted because of the growing dominance of the coupling with 2-4 level ISTs, resulting ultimately in the formation of the SHG spectral peak at a pump wavelength of 8.7 μm at -4 V. The electrically tunable SHG output spectra were simulated for the -2V shifted bias voltage ranging from -6 V to +2 V, as shown in Supplementary Fig. 10, and exhibited close agreement with the experimental spectra. The simulation result for M1 meta-atom array shows broader SHG spectral tuning than the measurement because the simulation assumed a uniform conduction band bending over the depth of the 400-nm-thick MQW layer. However, due to the formation of the Schottky contacts in the fabricated metasurface, major band bending occurs near the top MQW surface for a negative bias and near the bottom MQW surface for a positive bias. In this configuration, the modal overlap factor for the SHG is induced strongly near the top MQW surface, resulting in dominant SHG spectral tuning for negative biases (see Supplementary Fig. 11). We note that when ohmic contacts are formed at both sides of the MQW layer, even broader SHG spectral tuning can be achieved with a single meta-atom array. The measured SH peak power as a function of squared input peak power and squared input peak intensity for the three metasurfaces at their optimal operating pump wavelengths at 0 V are shown in Figs. 5c-e, with the corresponding SHG power conversion efficiencies as a function of input pump power and intensity shown in Figs. 5f-h. The three metasurfaces exhibit a SHG power conversion efficiency exceeding 0.02 % with an input pump

peak power of 180 mW and a peak intensity of 80 kW cm⁻². For the M1 metasurface at the equivalent pump power, an SHG conversion efficiency of 0.082% corresponding to an SHG peak power of 148 μW was achieved. The nonlinear conversion factor $\eta = P_{SH} / (P_{pump})^2$ for the three metasurfaces at low (high) pump intensity was 10.3 (2.8) mW W⁻² for the M1 metasurface, 2.4 (0.8) mW W⁻² for the M2 metasurface, and 2.2 (0.6) mW W⁻² for the M3 metasurface. At a pump intensity above 25 kW cm⁻², the slope of the SHG conversion efficiency curve decreases owing to the SHG intensity saturation effect⁴⁶. The peak SHG conversion efficiency values for the three metasurfaces according to the bias voltage are provided in Supplementary Fig. 12.

Using the electrically tunable nonlinear metasurface, it is also possible to achieve dynamic modulation of the SHG signal according to the applied AC modulation voltage at a fixed pump wavelength. Fig. 6a shows the SHG conversion efficiency spectra of the M1 metasurface for three different DC bias voltages, exhibiting the largest SHG signal modulation at a wavelength of 10.5 μm. In experiments, a square-shaped voltage pulse in the range from -2 V to -4 V with a frequency of 1 MHz was applied to the M1 metasurface, as shown in the top panel of Fig. 6b. In addition, a CO₂ laser in continuous wave mode with operating wavelength of 10.6 μm was used as the input pump source in conjunction with a mercury cadmium telluride (MCT) detector with a 3-ns response time. The bottom panel of Fig. 6b shows the output signal of the MCT detector monitored by an oscilloscope, exhibiting the exact form of the modulated SHG signal in response to the input voltage pulse. The RC time constant calculated by considering the device dimensions in the modulated voltage range was 145 ps, corresponding to a cut-off SHG modulation frequency of 1.09 GHz (see Supplementary Fig. 9 with accompanying discussion).

Discussion

In summary, we proposed and experimentally demonstrated electrically tunable nonlinear metasurfaces for broadband efficient SHG and a strong SH signal modulation based on the Stark tuning of intersubband nonlinearity. The energy levels of the electron subbands in the coupled three quantum well structure are modulated by the QCSE according to the bias voltage, leading to a broadband and giant 2nd order nonlinear response in the 8-11 μm wavelength range. Our approach can be extended to other nonlinear optical processes, such as sum- and difference-frequency generation and THG, and can also be applied to near-IR⁴⁷ and visible⁴⁸ wavelength applications by using different material compositions capable of inducing larger conduction band offsets. The nonlinear metasurfaces proposed here provide a new platform that can expand the design space of nonlinear flat optics significantly, owing to its ability to electrically tune the giant nonlinear response at the individual nanoresonators level. Moreover, they provide a new pathway to implement innovative meta-devices, such as electrically tunable broadband nonlinear light sources, active nonlinear beam-manipulation, electrically tunable nonlinear holography, and ultrafast nonlinear signal switching and modulation.

Methods

MQW design and characterization. The coupled three quantum well unit structure with the $\text{In}_{0.53}\text{Ga}_{0.47}\text{As}/\text{Al}_{0.48}\text{In}_{0.52}\text{As}$ heterostructure was designed by using a self-consistent Poisson-Schrodinger solver. The IST energies and their dipole moment elements according to the applied bias voltage were calculated using this solver. The layer sequence of the quantum well unit structure is **4/4.6/1.2/2/1.2/1.8/4** in nanometres where the boldface indicates the $\text{Al}_{0.48}\text{In}_{0.52}\text{As}$ barriers and $4 \times 10^{18} \text{ cm}^{-3}$ n-doping was injected into the 4.6 nm quantum well. For sample growth, a 300-nm-thick $\text{In}_{0.53}\text{Ga}_{0.47}\text{As}$ etch stop layer and a 100-nm-thick InP etch stop layer were grown

on a semi-insulating InP substrate; subsequently, the unit quantum well structure was repeated 20 times to form an MQW layer with a total thickness of 400 nm. Intersubband absorption measurement was performed using a multipath sample piece polished at an angle of 45 degrees on both sides. Using this measurement, IST energies ($E_{12} = \hbar\omega_{12} \approx 113 \text{ meV}$, $E_{23} = \hbar\omega_{23} \approx 135 \text{ meV}$, $E_{13} = \hbar\omega_{13} \approx 241 \text{ meV}$, $E_{14} = \hbar\omega_{14} \approx 340 \text{ meV}$), transition linewidths ($2\hbar\gamma_{12} \approx 20.8 \text{ meV}$, $2\hbar\gamma_{23} \approx 17.6 \text{ meV}$, $2\hbar\gamma_{13} \approx 28.4 \text{ meV}$, $2\hbar\gamma_{14} \approx 28.2 \text{ meV}$), and average electron density ($N_{e,1} \approx 3.5 \times 10^{18} \text{ cm}^{-3}$, $N_{e,2} \approx 0.5 \times 10^{18} \text{ cm}^{-3}$) in the MQW were extracted. For the calculation of the 2nd order nonlinear responses, $\chi_{zzz,1-3}^{(2)}$ and $\chi_{zzz,2-4}^{(2)}$, we used equation (1) and the following

$$\text{equation: } \chi_{zzz,2-4}^{(2)}(V) \approx \frac{e^3 N_{e,2}}{\epsilon_0} \frac{z_{23}(V)z_{34}(V)z_{42}(V)}{(\hbar\omega_{24}(V) - 2\hbar\omega - i\hbar\gamma_{24})(\hbar\omega_{23}(V) - \hbar\omega - i\hbar\gamma_{23})}, \text{ respectively,}$$

which were informed by the transition dipole moment elements and IST energies from the Poisson-Schrodinger calculation, and the averaged doping density and linewidths from the intersubband absorption measurement. The linewidth for the 2-4 level transition was assumed to be $\hbar\gamma_{24} = 15 \text{ meV}$.

Numerical simulation. For the meta-atom simulation, we used a finite-difference time-domain solver (Lumerical FDTD). The meta-atom structure shown in Fig. 3a was designed by applying periodic boundary conditions in the x - and y -directions and the perfect matched layer condition in the z -direction. The Au layer was modelled as a Drude metal with a plasma frequency of $\omega_p = 1.378 \times 10^{16} \text{ rad/s}$ and a collision frequency of $\Gamma = 1.224 \times 10^{14} \text{ rad/s}$. The MQW layer was modelled as a homogeneous anisotropic medium with the out-of-plane and in-plane dielectric constants, $\epsilon_{\perp}(\omega)$ and $\epsilon_{\parallel}(\omega)$, respectively (see Supplementary Information for details). There is a slight discrepancy between the design value and the measured value of the IST energies;

therefore, the electrically tunable linear and nonlinear response simulations of the metasurface were conducted in the -2 V shifted voltage range from +2 V to -6 V. The measured IST energies were used for the 0 V reflection spectra simulation shown in Fig. 3g, and the values from the Poisson-Schrodinger solver were used for the electrically tunable linear and nonlinear response simulations.

Device fabrication. To transfer the MQW layer onto the metal ground plane, 20 nm of Cr, 50 nm of Pt and 150 nm of Au layer were deposited on the MQW-layer-grown InP wafer and an Si wafer, then thermo-compression wafer bonding was implemented by placing the metal layers of the two wafers in contact with each other. The InP substrate was removed by mechanical polishing and selective chemical etching; subsequently, the 300-nm-thick InGaAs and 100-nm-thick InP etch stop layers were removed by selective chemical etching. The patterned Au nanoantenna and MQW layer were formed by electron-beam evaporation of 10 nm of Cr and 50 nm of Au layer, 400 nm of SiO₂ layer deposition by RF sputter, electron-beam lithography, and a two-step reactive-ion etching process, followed by SiO₂ layer removal in buffered oxide etchant. A mesa structure with $200 \times 200 \mu\text{m}^2$ size was formed to prevent current spreading and a 400-nm-thick SiN passivation layer was deposited on the sample by plasma-enhanced chemical vapor deposition. After forming a pattern opening, a Cr(20 nm)/Cu(300 nm)/Cr(10 nm)/Au(50 nm) top contact layer was patterned. Finally, the sample was mounted on a Cu plate using an Ag paste. The device fabrication process is illustrated in Supplementary Fig. 3.

Optical characterization. Linear reflection spectra of the metasurfaces were measured by FTIR equipped with an IR microscope (Bruker, vertex 70 and hyperion 1000). For nonlinear optical characterization, a broadly wavelength-tunable quantum cascade laser (QCL) in pulse mode (Daylight Solutions Inc., Mircat system, tuning range: 909 – 1230 cm⁻¹, peak power: 400 mW,

repetition rate: 100 kHz, duty cycle: 10%) and a calibrated InSb photodetector (Electro Optical System, Inc.,) were used as shown in Fig. 5a. The linearly polarized input beam from the QCL passes through the dichroic beam splitter (pass wavelength: $> 7 \mu\text{m}$) and focuses on the metasurface by the ZnSe objective lens (numerical aperture: 0.25). The generated SH signal is directed to the detector via the LP filter, the linear polarizer, the ZnSe lens, and the short-pass (SP) filter (cut-off wavelength: $6 \mu\text{m}$). The focal spot diameter at the sample position was $2w = 25 \mu\text{m}$, confirmed by the Knife-edge measurement. A Gaussian power profile was assumed both for the FF input pump beam ($P_{FF} = I_{FF} e^{-2r^2/w^2}$) and the SH beam ($P_{SH} = I_{SH} e^{-4r^2/w^2}$). The average pump power was measured by a thermal power meter (Thorlabs, S302C). The DC bias voltage was applied using a source meter (Keithley, SMU 2450). For dynamic SHG signal modulation, a CO₂ laser (Coherent, diamond c-55) in continuous wave mode with operating wavelength of $10.6 \mu\text{m}$ and a TE-cooled MCT photodetector (Daylight solutions, HPC-2TE-100) with a 3-ns response time were used. The MCT detector gives negative output voltage for the collected light. The square voltage pulse was applied using a high voltage pulse generator (HP, 8114A).

REFERENCES

1. Yu, N. F., Capasso, F. Flat optics with designer metasurfaces. *Nat Mater*, **13**, 139-150 (2014).
2. Shaltout, A. M., Shalaei, V. M., Brongersma, M. L. Spatiotemporal light control with active metasurfaces. *Science*, **364**, 648 (2019).
3. Lee, J., Jung, S., Chen, P. Y., Lu, F., Demmerle, F., Boehm, G., *et al.* Ultrafast Electrically Tunable Polaritonic Metasurfaces. *Adv Opt Mater*, **2**, 1057-1063 (2014).
4. Park, J., Kang, J. H., Kim, S. J., Liu, X. G., Brongersma, M. L. Dynamic Reflection Phase and Polarization Control in Metasurfaces. *Nano Lett*, **17**, 407-413 (2017).
5. Sherrott, M. C., Hon, P. W. C., Fountaine, K. T., Garcia, J. C., Ponti, S. M., Brar, V. W., *et al.* Experimental Demonstration of > 230 degrees Phase Modulation in Gate-Tunable Graphene-Gold Reconfigurable Mid-Infrared Metasurfaces. *Nano Lett*, **17**, 3027-3034 (2017).
6. Huang, Y. W., Lee, H. W. H., Sokhoyan, R., Pala, R. A., Thyagarajan, K., Han, S., *et al.* Gate-Tunable Conducting Oxide Metasurfaces. *Nano Lett*, **16**, 5319-5325 (2016).
7. Wan, X., Qi, M. Q., Chen, T. Y., Cui, T. J. Field-programmable beam reconfiguring based on digitally-controlled coding metasurface. *Sci Rep*, **6** (2016).
8. Shirmanesh, G. K., Sokhoyan, R., Wu, P. C., Atwater, H. A. Electro-optically Tunable Multifunctional Metasurfaces. *ACS Nano*, **14**, 6912-6920 (2020).
9. Li, L. L., Cui, T. J., Ji, W., Liu, S., Ding, J., Wan, X., *et al.* Electromagnetic reprogrammable coding-metasurface holograms. *Nat Commun*, **8**, 197 (2017).
10. Tymchenko, M., Gomez-Diaz, J. S., Lee, J., Nookala, N., Belkin, M. A., Alu, A. Gradient Nonlinear Pancharatnam-Berry Metasurfaces. *Phys Rev Lett*, **115**, 207403 (2015).

11. Nookala, N., Lee, J., Tymchenko, M., Gomez-Diaz, J. S., Demmerle, F., Boehm, G., *et al.* Ultrathin gradient nonlinear metasurface with a giant nonlinear response. *Optica*, **3**, 283-288 (2016).
12. Li, G., Zhang, S., Zentgraf, T. Nonlinear photonic metasurfaces. *Nat Rev Mater*, **2** (2017).
13. Krasnok, A., Tymchenko, M., Alu, A. Nonlinear metasurfaces: a paradigm shift in nonlinear optics. *Mater Today*, **21**, 8-21 (2018).
14. Almeida, E., Bitton, O., Prior, Y. Nonlinear metamaterials for holography. *Nat Commun*, **7**, 12533 (2016).
15. Ye, W. M., Zeuner, F., Li, X., Reineke, B., He, S., Qiu, C. W., *et al.* Spin and wavelength multiplexed nonlinear metasurface holography. *Nat Commun*, **7**, 11930 (2016).
16. Dasgupta, A., Gao, J., Yang, X. D. Atomically Thin Nonlinear Transition Metal Dichalcogenide Holograms. *Nano Lett*, **19**, 6511-6516 (2019).
17. Reineke, B., Sain, B., Zhao, R. Z., Carletti, L., Liu, B. Y., Huang, L. L., *et al.* Silicon Metasurfaces for Third Harmonic Geometric Phase Manipulation and Multiplexed Holography. *Nano Lett*, **19**, 6585-6591 (2019).
18. Schlickriede, C., Kruk, S. S., Wang, L., Sain, B., Kivshar, Y., Zentgraf, T. Nonlinear Imaging with All-Dielectric Metasurfaces. *Nano Lett*, **20**, 4370-4376 (2020).
19. Walter, F., Li, G. X., Meier, C., Zhang, S., Zentgraf, T. Ultrathin Nonlinear Metasurface for Optical Image Encoding. *Nano Lett*, **17**, 3171-3175 (2017).
20. Ma, M. L., Li, Z., Liu, W. W., Tang, C. C., Li, Z. C., Cheng, H., *et al.* Optical Information Multiplexing with Nonlinear Coding Metasurfaces. *Laser Photonics Rev*, **13**, 1900045 (2019).
21. Tang, Y. T., Intaravanne, Y., Deng, J. H., Li, K. F., Chen, X. Z., Li, G. X. Nonlinear Vectorial Metasurface for Optical Encryption. *Phys Rev Appl*, **12**, 024028 (2019).

22. Shcherbakov, M. R., Vabishchevich, P. P., Shorokhov, A. S., Chong, K. E., Choi, D. Y., Staude, I., *et al.* Ultrafast All-Optical Switching with Magnetic Resonances in Nonlinear Dielectric Nanostructures. *Nano Lett*, **15**, 6985-6990 (2015).
23. Lu, C. C., Hu, X. Y., Shi, K. B., Hu, Q., Zhu, R., Yang, H., *et al.* An actively ultrafast tunable giant slow-light effect in ultrathin nonlinear metasurfaces. *Light-Sci Appl*, **4**, e302 (2015).
24. Klein, M. W., Enkrich, C., Wegener, M., Linden, S. Second-harmonic generation from magnetic metamaterials. *Science*, **313**, 502-504 (2006).
25. Celebrano, M., Wu, X. F., Baselli, M., Grossmann, S., Biagioni, P., Locatelli, A., *et al.* Mode matching in multiresonant plasmonic nanoantennas for enhanced second harmonic generation. *Nat Nanotechnol*, **10**, 412-417 (2015).
26. Segal, N., Keren-Zur, S., Hendler, N., Ellenbogen, T. Controlling light with metamaterial-based nonlinear photonic crystals. *Nat Photon*, **9**, 180-184 (2015).
27. Yang, Y. M., Wang, W. Y., Boulesbaa, A., Kravchenko, I. I., Briggs, D. P., Puretzky, A., *et al.* Nonlinear Fano-Resonant Dielectric Metasurfaces. *Nano Lett*, **15**, 7388-7393 (2015).
28. Liu, S., Vabishchevich, P. P., Vaskin, A., Reno, J. L., Keeler, G. A., Sinclair, M. B., *et al.* An all-dielectric metasurface as a broadband optical frequency mixer. *Nat Commun*, **9**, 2507 (2018).
29. Wang, L., Kruk, S., Koshelev, K., Kravohenk, I., Luther-Davies, B., Kivshar, Y. Nonlinear Wavefront Control with All-Dielectric Metasurfaces. *Nano Lett*, **18**, 3978-3984 (2018).
30. Koshelev, K., Kruk, S., Melik-Gaykazyan, E., Choi, J. H., Bogdanov, A., Park, H. G., *et al.* Subwavelength dielectric resonators for nonlinear nanophotonics. *Science*, **367**, 288 (2020).
31. Cai, W. S., Vasudev, A. P., Brongersma, M. L. Electrically Controlled Nonlinear Generation of Light with Plasmonics. *Science*, **333**, 1720-1723 (2011).

32. Kang, L., Cui, Y. H., Lan, S. F., Rodrigues, S. P., Brongersma, M. L., Cai, W. S. Electrifying photonic metamaterials for tunable nonlinear optics. *Nat Commun*, **5**, 4680 (2014).
33. Ding, W., Zhou, L. C., Chou, S. Y. Enhancement and Electric Charge-Assisted Tuning of Nonlinear Light Generation in Bipolar Plasmonics. *Nano Lett*, **14**, 2822-2830 (2014).
34. Lee, K. T., Taghinejad, M., Yan, J. H., Kim, A. S., Raju, L., Brown, D. K., *et al.* Electrically Biased Silicon Metasurfaces with Magnetic Mie Resonance for Tunable Harmonic Generation of Light. *ACS Photon*, **6**, 2663-2670 (2019).
35. Lee, J., Tymchenko, M., Argyropoulos, C., Chen, P. Y., Lu, F., Demmerle, F., *et al.* Giant nonlinear response from plasmonic metasurfaces coupled to intersubband transitions. *Nature*, **511**, 65-69 (2014).
36. Wolf, O., Campione, S., Benz, A., Ravikumar, A. P., Liu, S., Luk, T. S., *et al.* Phased-array sources based on nonlinear metamaterial nanocavities. *Nat Commun*, **6**, 7667 (2015).
37. Lee, J., Nookala, N., Gomez-Diaz, J. S., Tymchenko, M., Demmerle, F., Boehm, G., *et al.* Ultrathin Second-Harmonic Metasurfaces with Record-High Nonlinear Optical Response. *Adv Opt Mater*, **4**, 664-670 (2016).
38. Nookala, N., Xu, J. M., Wolf, O., March, S., Sarma, R., Bank, S., *et al.* Mid-infrared second-harmonic generation in ultra-thin plasmonic metasurfaces without a full-metal backplane. *Appl Phys B*, **124**, 132 (2018).
39. Yu, J., Park, S., Hwang, I., Kim, D., Jung, J. Y., Lee, J. Third-Harmonic Generation from Plasmonic Metasurfaces Coupled to Intersubband Transitions. *Adv Opt Mater*, **7**, 1801510 (2019).

40. Kim, D., Chung, H. J., Yu, J. Y., Hwang, I., Park, S., Demmerle, F., *et al.* Spin-Controlled Nonlinear Harmonic Generations from Plasmonic Metasurfaces Coupled to Intersubband Transitions. *Adv Opt Mater*, **8**, 2000004 (2020).
41. Rosencher, E., Fiore, A., Vinter, B., Berger, V., Bois, P., Nagle, J. Quantum engineering of optical nonlinearities. *Science*, **271**, 168-173 (1996).
42. Sirtori, C., Capasso, F., Sivco, D. L., Hutchinson, A. L., Cho, A. Y. Resonant Stark Tuning of 2nd-Order Susceptibility in Coupled Quantum-Wells. *Appl Phys Lett*, **60**, 151-153 (1992).
43. Boyd, R. W. *Nonlinear Optics*. Academic, (2008).
44. Balanis, C. A. *Advanced Engineering Electromagnetics*. Wiley, (1989).
45. Todorov, Y., Andrews, A. M., Colombelli, R., De Liberato, S., Ciuti, C., Klang, P., *et al.* Ultrastrong Light-Matter Coupling Regime with Polariton Dots. *Phys Rev Lett*, **105**, 196402 (2010).
46. Gomez-Diaz, J. S., Tymchenko, M., Lee, J., Belkin, M. A., Alu, A. Nonlinear processes in multi-quantum-well plasmonic metasurfaces: Electromagnetic response, saturation effects, limits, and potentials. *Phys Rev B*, **92**, 125429 (2015).
47. Wolf, O., Allerman, A. A., Ma, X., Wendt, J. R., Song, A. Y., Shaner, E. A., *et al.* Enhanced optical nonlinearities in the near-infrared using III-nitride heterostructures coupled to metamaterials. *Appl Phys Lett*, **107**, 151108 (2015).
48. Qian, H. L., Li, S. L., Chen, C. F., Hsu, S. W., Bopp, S. E., Ma, Q., *et al.* Large optical nonlinearity enabled by coupled metallic quantum wells. *Light-Sci Appl*, **8**, 13 (2019).

Acknowledgements

This work was supported by a Basic Science Research Program and Nano-Material Technology Development Program through the National Research Foundation of Korea (NRF) grants funded by the Korea government (MSIT) (Nos. 2019R1A2C4070623, 2020R1A4A3079834, and 2018M3A7B4069995). This paper is dedicated to the memory of Prof. Markus-Christian Amann who supervised the growth of the semiconductor heterostructure used in this study. Prof. Amann passed away unexpectedly on November 23, 2018.

Author Contributions

J.Y. designed the semiconductor heterostructure and calculated the physical parameters. F.D., G.B., M.C.A., and M.A.B. performed the semiconductor heterostructure growth. J. Y. fabricated the device and performed all experimental measurements and simulations. S.P. assisted with the meta-atom design and simulations. I.H. and D.K. assisted with the device fabrication and measurement. J.L. conceived and developed the concept and directed the research. J.Y., M.A.B., and J.L. wrote the manuscript.

Competing interests

The authors declare no competing interest.

Figures and Figure legends

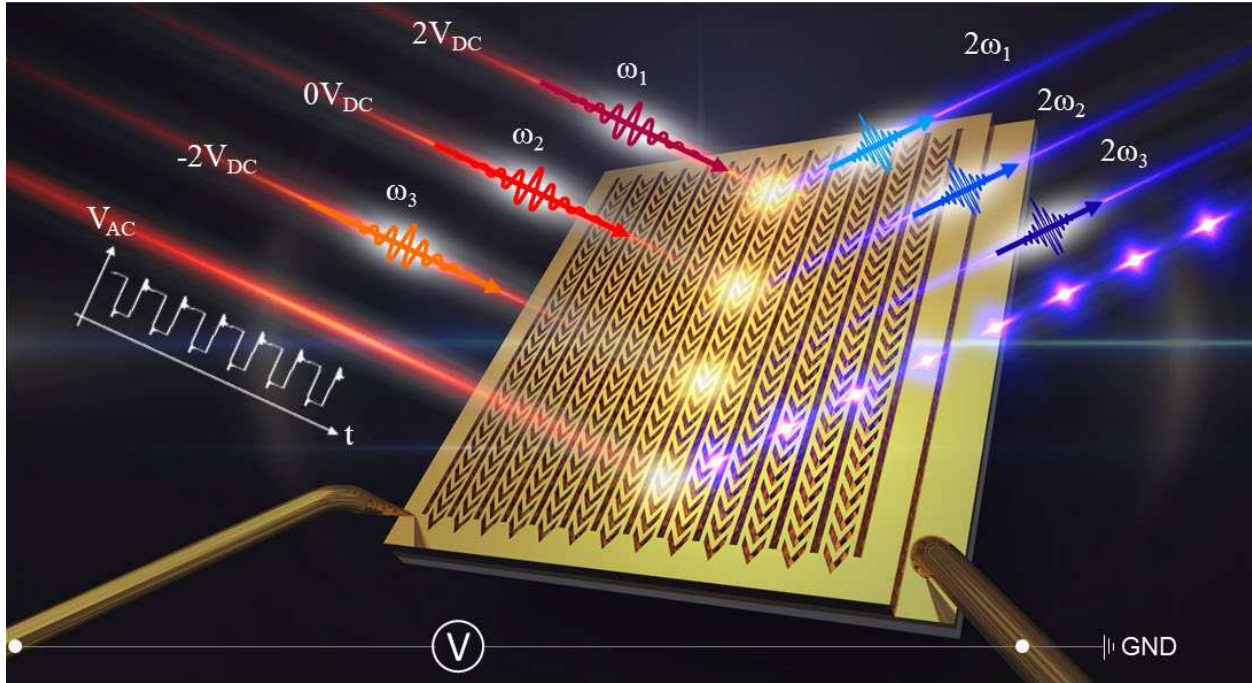


Fig. 1 | Concept of the electrically tunable nonlinear metasurface. The metasurface consists of an array of plasmonic nanocavity with an MQW layer inserted. The MQW layer was designed to have the giant 2nd order nonlinear response for SHG, with its maximum nonlinear response spectrally tuned by the applied bias voltage, thus producing a broadband giant nonlinear response. For positive and negative DC bias voltages applied to the device, the maximum SHG occurs at higher and lower pump frequencies ($\omega_1 > \omega_2 > \omega_3$), respectively. When a voltage pulse is applied to the device, strong SHG signal modulation is induced at a fix pump frequency.

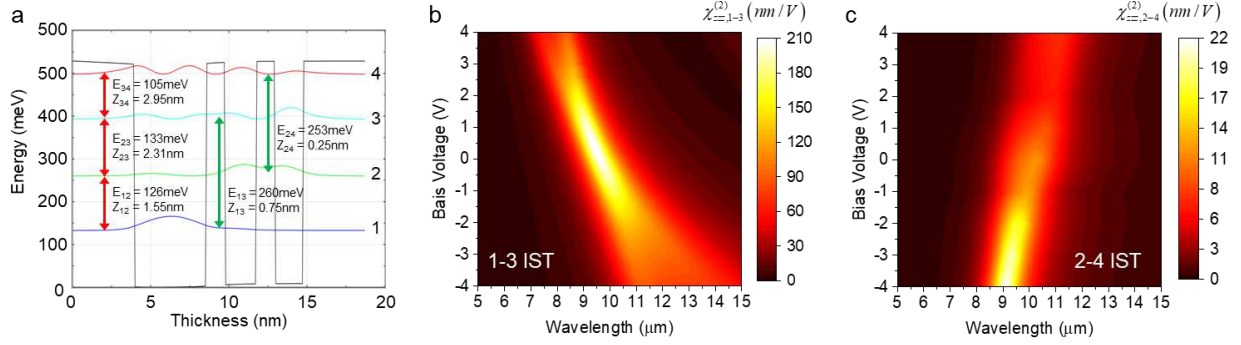


Fig. 2 | MQW design and electrically tunable 2nd order nonlinear response. **a**, Conduction band diagram for the $\text{In}_{0.53}\text{Ga}_{0.47}\text{As}/\text{Al}_{0.48}\text{In}_{0.52}\text{As}$ coupled three-quantum-well unit structure under zero bias voltage, where E_{ij} and z_{ij} indicate the energy separation and transition dipole element between electron state i and j , respectively. **b,c**, Calculated 2nd order nonlinear susceptibility of the MQW structure produced by the ISTs between electron subbands 1-3 (**b**, $\chi_{zz,1-3}^{(2)}$) and the ISTs between electron subbands 2-4 (**c**, $\chi_{zz,2-4}^{(2)}$) as functions of the input pump wavelengths (x -axis) and applied bias voltages (y -axis).

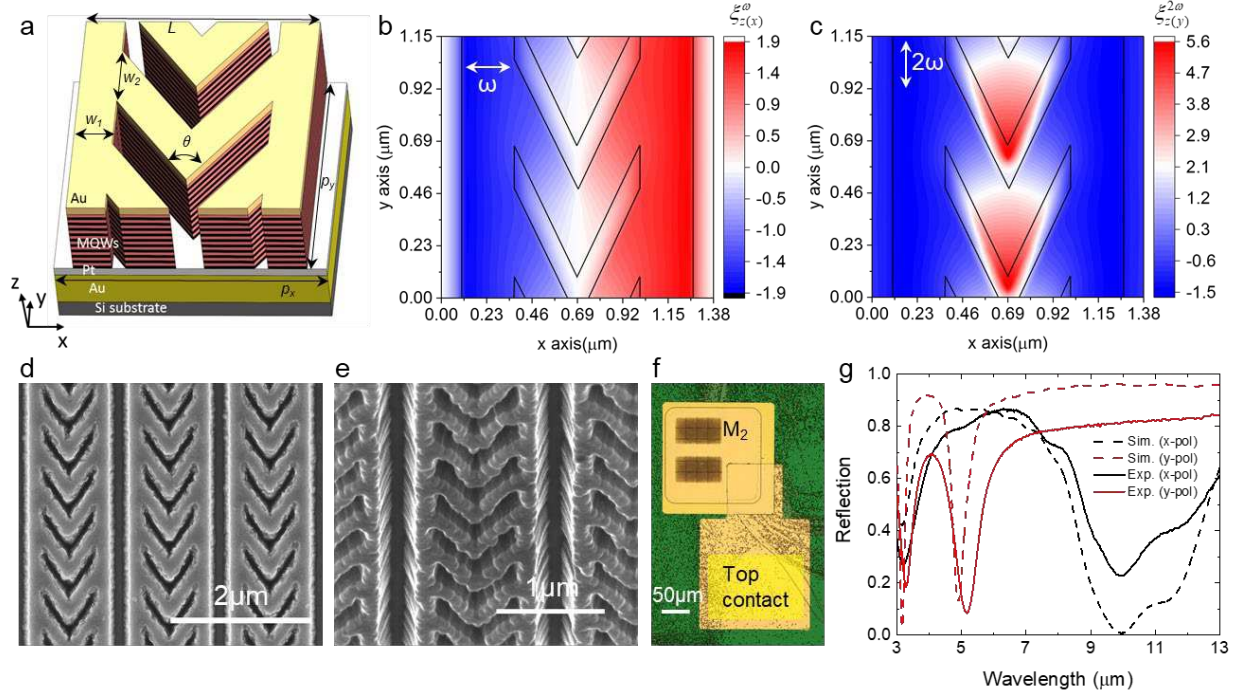


Fig. 3 | Numerical simulations of the meta-atom structure and fabricated metasurface. a, M2 meta-atom unit structure designed for SHG. The dimensions of the M2 meta-atom are: $w_1=270\text{nm}$, $w_2=380\text{nm}$, $p_x=1380\text{nm}$, $p_y=1150\text{nm}$, $L=1160\text{nm}$, and $\theta=57.6^\circ$. **b,c**, Top-down view cross-section of the normalized E_z field enhancement distribution at the FF with x -polarized input E-field (**b**, $\xi_{z(x)}^\omega = E_z^\omega / E_{x,inc}^\omega$) and at the SH frequency with y -polarized input E-field (**c**, $\xi_{z(y)}^{2\omega} = E_z^{2\omega} / E_{y,inc}^{2\omega}$). The E_z field enhancement was monitored at 100 nm below the top surface of the MQW layer. **d-f**, Scanning electron microscopy images (**d**: top-down view, **e**: 60° tilted view) and optical microscope image (**f**) of the fabricated metasurface. **g**, Simulated (dashed curve) and measured (solid curve) linear reflection spectra of the metasurface for x - (black) and y -polarized (red) light at normal incidence.

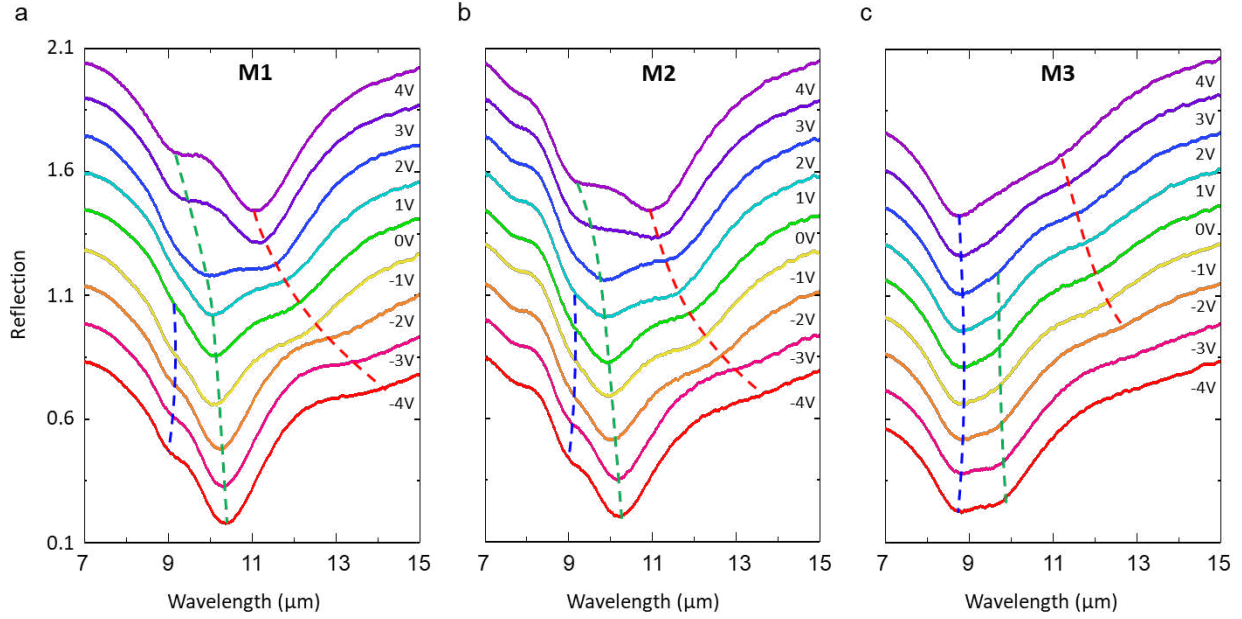


Fig. 4 | Experimental reflection spectra of the metasurfaces for different DC bias voltages. a-c, Reflection spectra of the three arrays of the meta-atom structures, **(a)** M1, **(b)** M2, and **(c)** M3 optimized to have plasmonic resonance at 10.5 μm , 9.8 μm , and 9.6 μm , respectively, under x -polarized incident light and a DC bias voltage ranging from -4 V to +4 V with 1 V step. For better display of the data, the reflection spectra at different bias voltages are offset from each other vertically by 0.15. The three dashed curves trace the positions of the three polaritonic peaks induced by the coupling of the plasmonic resonance, 1-2 level IST, and 2-3 level IST as the DC bias voltage changes.

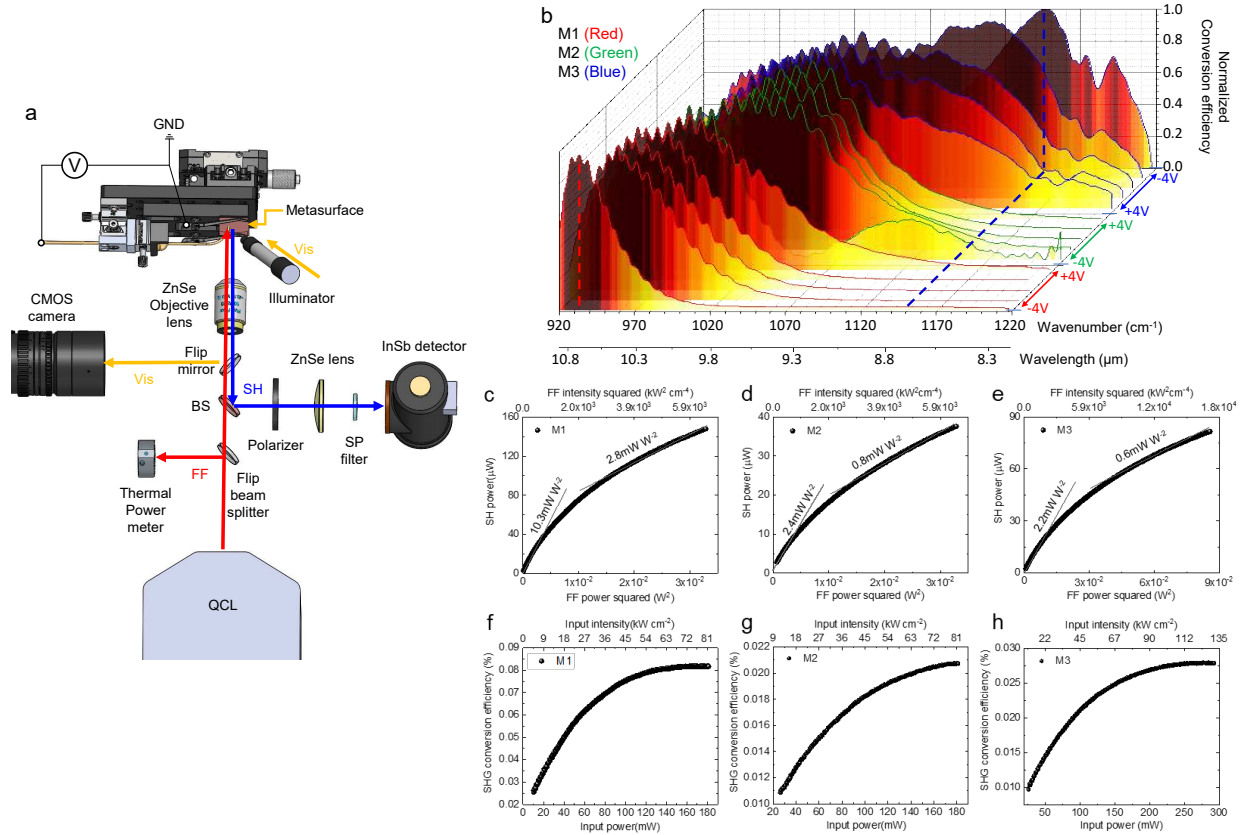


Fig. 5 | Nonlinear characterization of the electrically tunable metasurface. **a**, Optical setup for the measurement of the SHG signal from the metasurface under a DC bias voltage. The linearly polarized input beam at the FF (red arrow) from the quantum cascade laser (QCL) was focused onto the metasurface via the dichroic beam splitter (BS) and the ZnSe objective lens. The SH signal (blue arrow) generated from the device was collected by the same lens and directed to the InSb detector via the BS, linear polarizer, ZnSe lens, and short-pass (SP) filter. The flip mirror and the flip beam splitter were used only for the sample alignment and power monitoring, respectively, and they were removed when measuring the SHG signal. **b**, 3D plot of the measured SHG conversion efficiency spectra normalized to their maximum value as a function of the input pump wavenumber for different DC bias voltages from -4 V to +4 V with 2 V step. The conversion efficiency curves for the three metasurfaces are plotted using different colors. **c-e**, Measured SH

peak power as a function of the squared input pump power (bottom x -axis) or squared input intensity (top x -axis) for the metasurfaces (c) M1, (d) M2, and (e) M3 at pump wavelengths of 10.5, 9.8, and 9.6 μm , respectively. f-h, Measured SH power conversion efficiency as a function of the input pump power for the metasurfaces (f) M1, (g) M2, and (h) M3 at pump wavelength of 10.5, 9.8, and 9.6 μm , respectively.

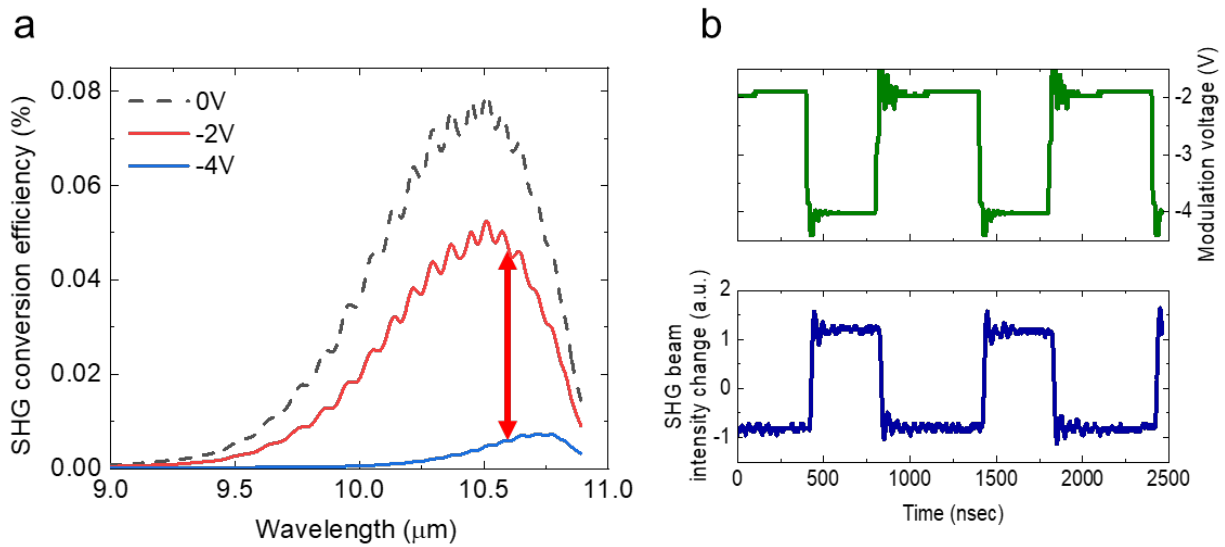


Fig. 6 | Dynamic modulation of the SHG signal. **a**, SHG power conversion efficiency spectra of the M1 metasurface under three DC bias voltages. SHG signal difference for -2 V and -4 V at a wavelength of 10.6 μm (CO_2 laser wavelength) is indicated by the red arrow. **b**, The square voltage pulse between -2 V and -4 V with 40% duty cycle used for the dynamic SHG signal modulation measurement (upper panel) and the modulated SHG signal (bottom panel) monitored at the output of the fast MCT detector with a 3-ns response time.

Figures

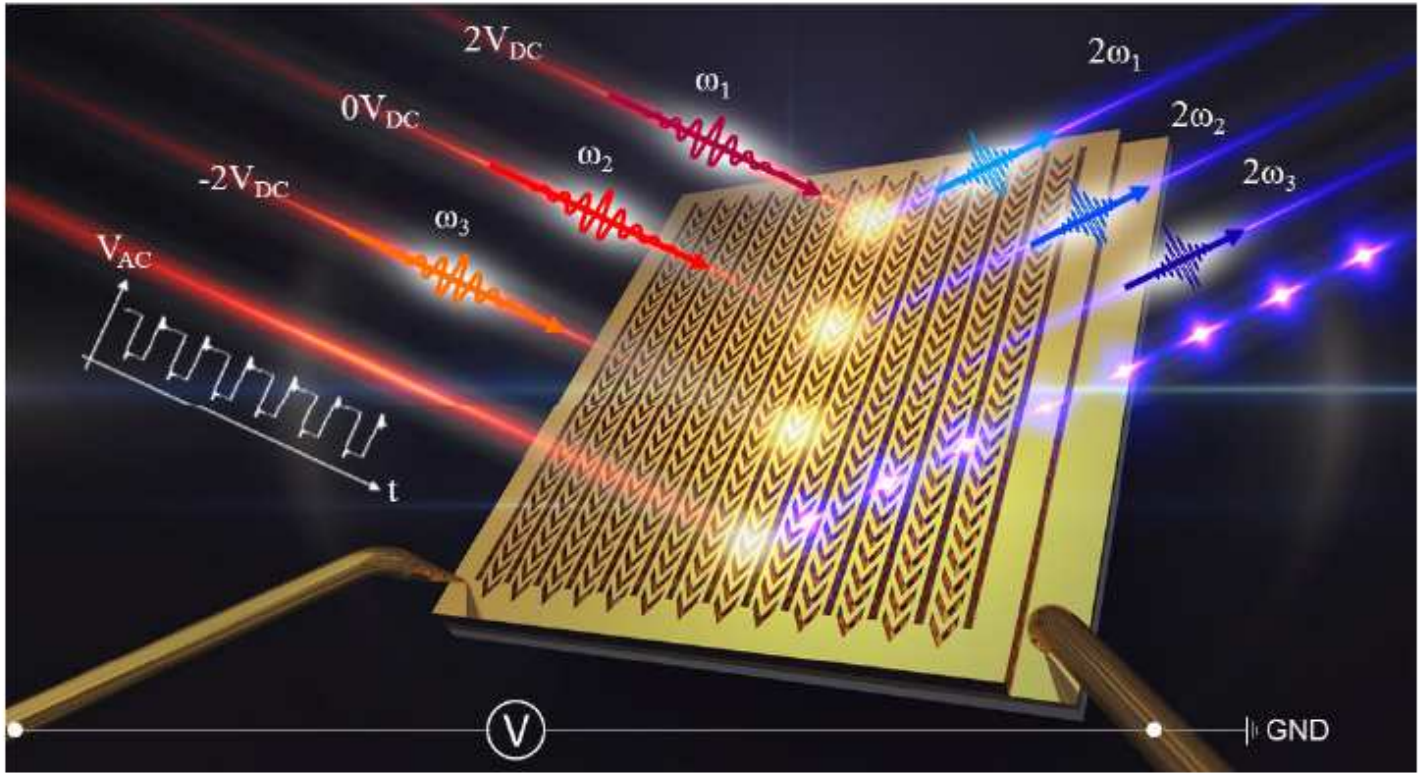


Figure 1

Concept of the electrically tunable nonlinear metasurface.

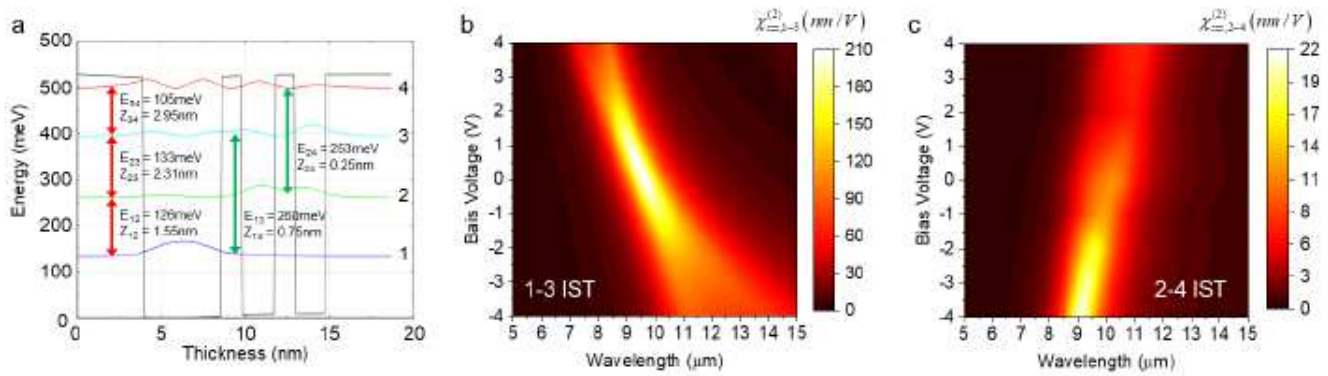


Figure 2

MQW design and electrically tunable 2nd order nonlinear response.

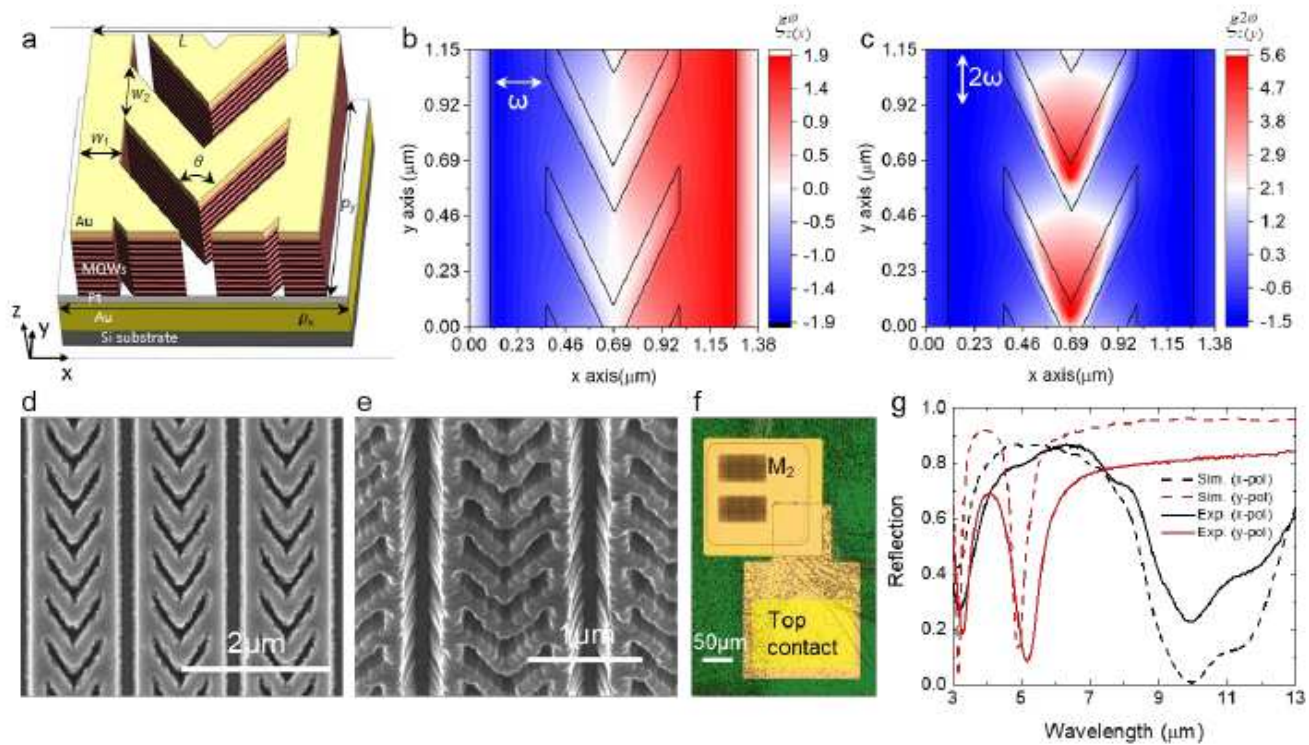


Figure 3

Numerical simulations of the meta-atom structure and fabricated metasurface.

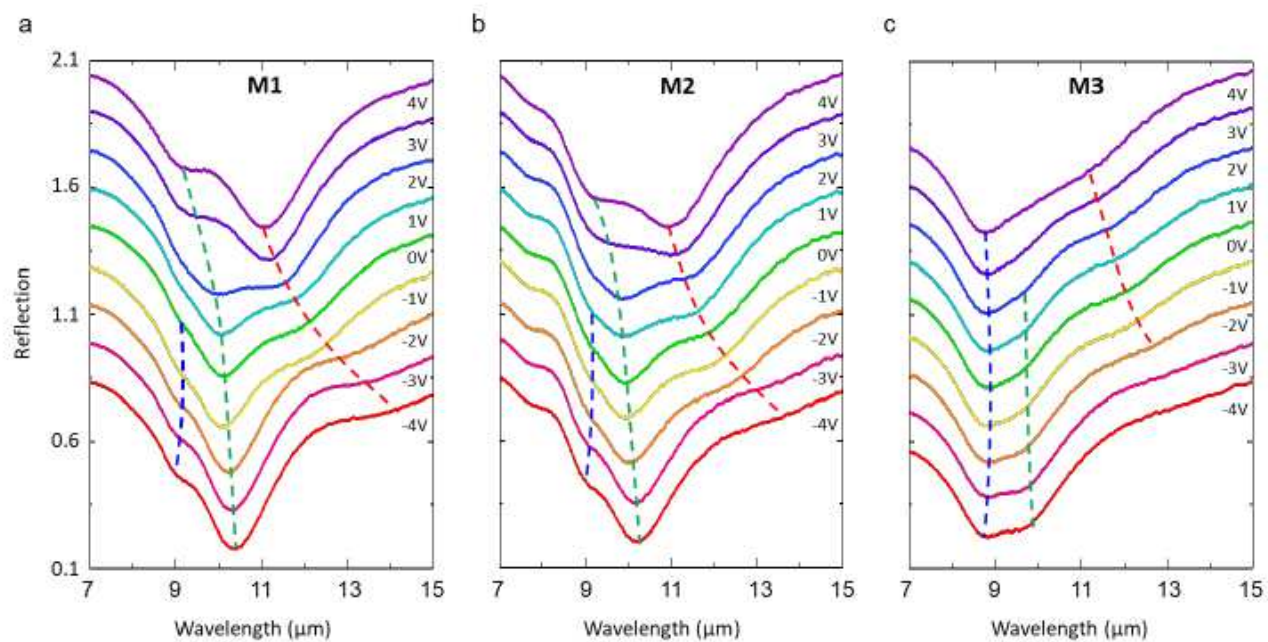


Figure 4

Experimental reflection spectra of the metasurfaces for different DC bias voltages

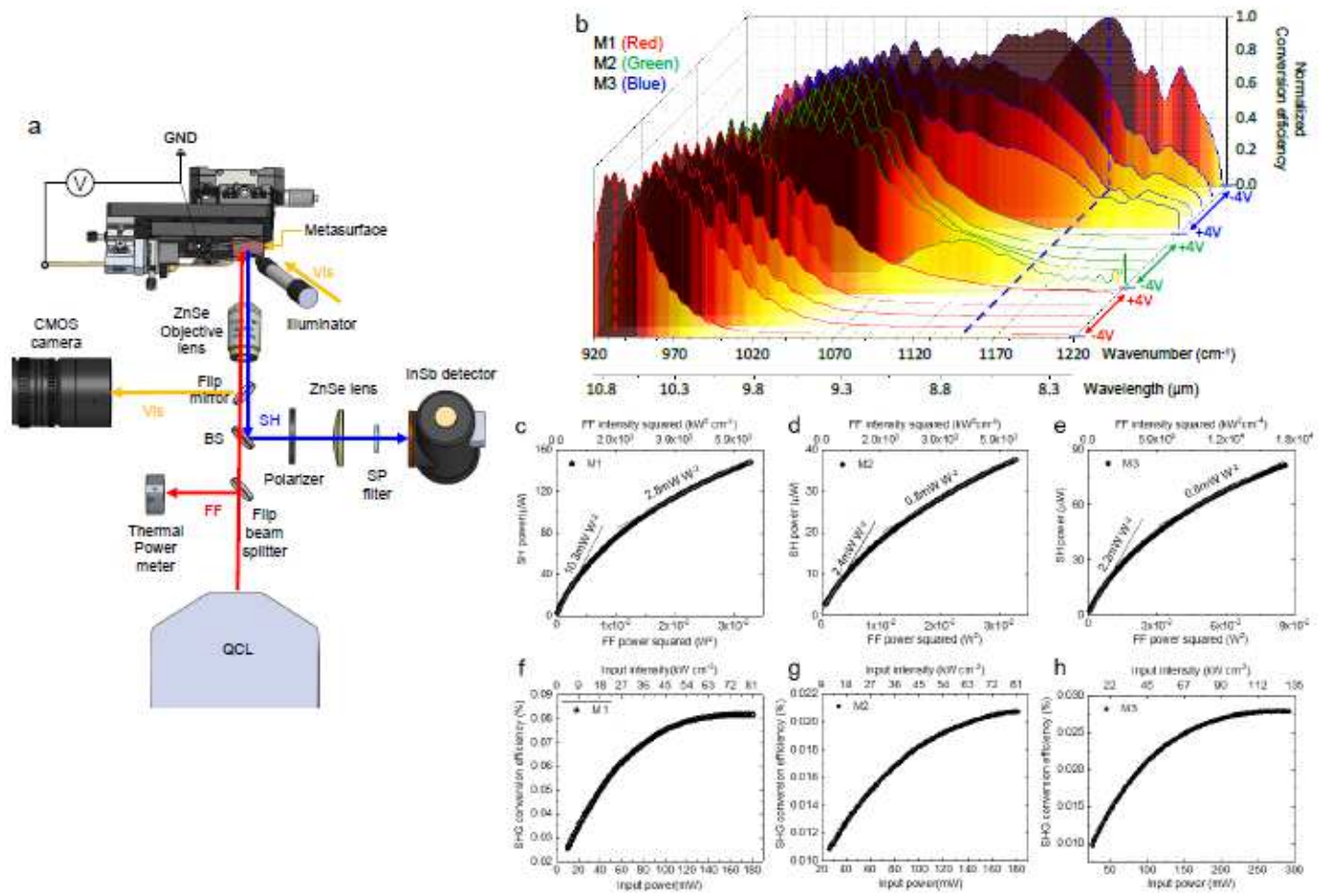


Figure 5

Nonlinear characterization of the electrically tunable metasurface

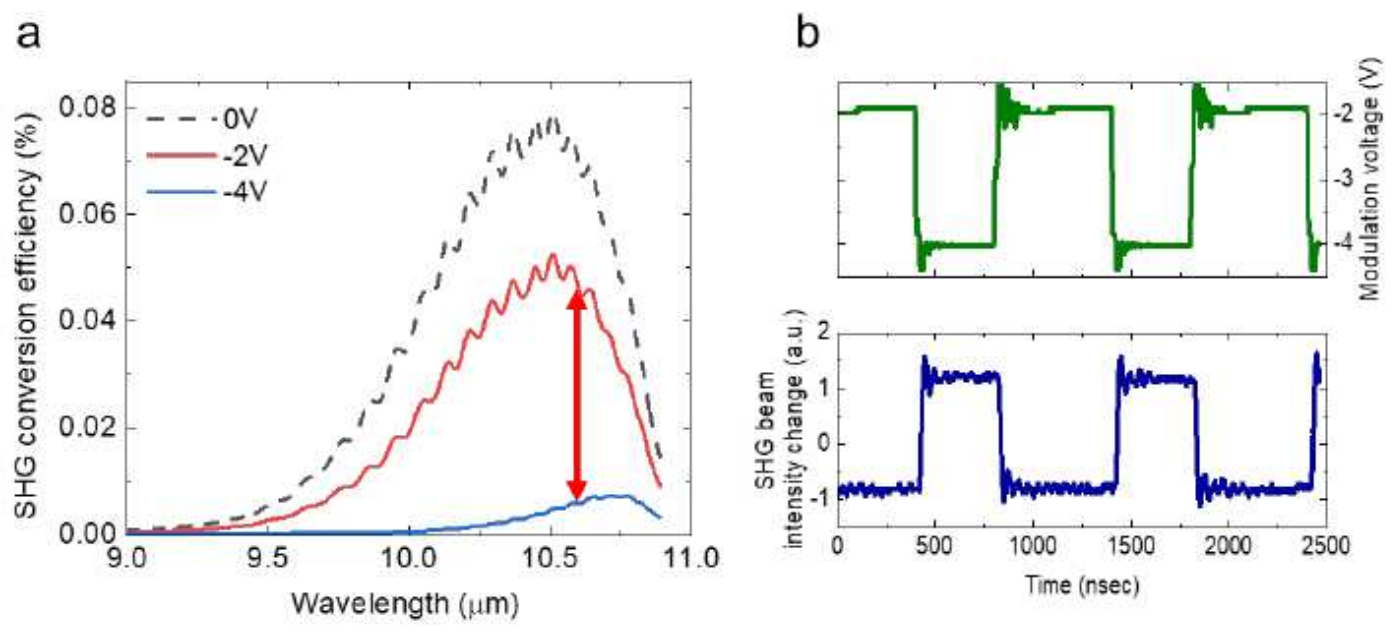


Figure 6

Dynamic modulation of the SHG signal

Supplementary Files

This is a list of supplementary files associated with this preprint. Click to download.

- [NatPhotonBroadbandSHGmetaSupplementInformationFinal.docx](#)
- [FigS1.png](#)
- [FigS2.png](#)
- [FigS3.png](#)
- [FigS4.png](#)
- [FigS5.png](#)
- [FigS6.png](#)
- [FigS7.png](#)
- [FigS8.png](#)
- [FigS9.png](#)
- [FigS10.png](#)
- [FigS11.png](#)
- [FigS12.png](#)
- [TableS1.png](#)